Technical Report TR-2015-09

Boundary condition enforcing methods for smoothed particle hydrodynamics

Arman Pazouki[1], Baofang Song[2], Dan Negrut[1]

[1]University of Wisconsin-Madison, Madison, WI, 53706-1572, USA
[2]Institute for Multiscale Simulation, Friedrich-Alexander-Universität Erlangen-Nürnberg, Nägelsbachstraße 49b, 91052 Erlangen, Germany

September 9, 2015

Abstract

A Boundary Condition Enforcing (BCE) marker approach is implemented in [9] to capture the fluid interaction with solid boundaries. BCE markers are treated there as fluid markers attached to solid surface. The velocity of each BCE marker is the same as the local solid velocity, while the pressure is obtained by projecting the fluid local pressure in the boundary normal direction. Alternatively, an approach was proposed recently [1] to improve the boundary accuracy by modifying the BCE velocity and pressure to reproduce the wall velocity and force balance at the boundary. These two approaches are compared herein.

Keywords: boundary condition enforcing markers, smoothed particle hydrodynamics, fluid-solid interaction, force balance

Contents

1 Smoothed Particle Hydrodynamics (SPH)

SPH is a Lagrangian method that probes the fluid domain at a set of moving markers. Each marker has an associated kernel function with compact support that is used to propagate marker state information over its domain of influence. The choice of kernel function W is not unique. A cubic spline interpolation kernel [7] was used in this work. At a point located by a position vector $\mathbf{r}$ with respect to an SPH marker, the cubic spline interpolation kernel is defined as

$$W(q,h) = \frac{1}{4\pi h^3} \times \begin{cases} (2-q)^3 - 4(1-q)^3, & 0 \le q < 1 \\ (2-q)^3, & 1 \le q < 2 \\ 0, & q \ge 2 \end{cases}, \tag{1}$$

where h is the kernel function's characteristic length and $q \equiv |\mathbf{r}|/h$. The radius of the support domain, κh, is proportional to the characteristic length h through the parameter κ which is equal to 2 for the cubic spline kernel.

Using the SPH framework, the continuity and momentum equations, given respectively by

$$\frac{d\rho}{dt} = -\rho \nabla \cdot \mathbf{v} \ , \tag{2}$$

and

$$\frac{d\mathbf{v}}{dt} = -\frac{1}{\rho}\nabla p + \frac{\mu}{\rho}\nabla^2 \mathbf{v} + \mathbf{f} \ , \tag{3}$$

are discretized as [8]

$$\frac{d\rho_a}{dt} = \rho_a \sum_b \frac{m_b}{\rho_b} \left(\mathbf{v}_a - \mathbf{v}_b\right) \cdot \nabla_a W_{ab} \ , \tag{4}$$

and

$$\frac{d\mathbf{v}_a}{dt} = -\sum_b m_b \left((\frac{p_a}{{\rho_a}^2} + \frac{p_b}{{\rho_b}^2}) \nabla_a W_{ab} - \frac{(\mu_a + \mu_b)\mathbf{x}_{ab} \cdot \nabla_a W_{ab}}{\bar{\rho}_{ab}^2 (x_{ab}^2 + \varepsilon \bar{h}_{ab}^2)} \mathbf{v}_{ab} \right) + \mathbf{f}_a \ . \tag{5}$$

In terms of notation, ρ and μ are the fluid density and viscosity, respectively; $\mathbf{v}$ and p are flow velocity and pressure, respectively; m is the mass associated with an SPH marker; $\mathbf{f}$ is the volumetric force; t is the real time; $\mathbf{x}_{ab}$ is the relative distance between markers a and b, i.e. $\mathbf{x}_{ab} = \mathbf{x}_a - \mathbf{x}_b$; $W_{ab} \equiv W|_{\mathbf{r}=\mathbf{x}_{ab}}$; ∇_a is gradient with respect to $\mathbf{x}_a$, i.e. $\partial/\partial \mathbf{x}_a$; quantities with over-bar are the average of the same quantities for markers a and b; ε is a regularization coefficient, and the summation is over all markers within the support domain of marker a.

The pressure p is evaluated using an equation of state [2, 3, 6]

$$p = \frac{{c_s}^2 \rho_0}{\gamma} \left\{ \left(\frac{\rho}{\rho_0} \right)^{\gamma} - 1 \right\}, \tag{6}$$

where ρ_0 is the reference density of the fluid, γ tunes the stiffness of the pressure-density relationship and normally has the value $\gamma = 7$, and c_s is the speed of sound. In the weakly compressible SPH method, c_s is adjusted depending on the maximum speed of the flow, $V_{\max}$, to keep the flow compressibility below any arbitrary value. Monaghan suggested the use of $c_s = 10V_{\max}$ for a compressibility less than 1% [6]. The analysis leading to this conclusion neglects the numerical artifacts introduced by the particle approximation of the fluid domain. In practice, a c_s larger than $10V_{\max}$ may be required. This, however, comes at the expense of smaller integration time steps.

The fluid flow equations, Eqs. (4) and (5), are solved in conjunction with Eq. (7) to update the position of the SPH markers:

$$\frac{d\mathbf{x}_a}{dt} = \mathbf{v}_a. \tag{7}$$

Finally, we employ the extended SPH approach, XSPH, which prevents extensive overlap of markers support domain and enhances incompressibility of the flow [5]. This correction takes into account the velocity of neighboring markers through a mean velocity evaluated within the support of a nominal marker a as

$$\langle \mathbf{v}_a \rangle = \mathbf{v}_a + \zeta \sum_b \frac{m_b}{\bar{\rho}_{ab}} (\mathbf{v}_b - \mathbf{v}_a) W_{ab}, \tag{8}$$

where $0 \leq \zeta \leq 1$ adjusts the contribution of the neighbors' velocities.

Recently, Adami *et* al. [1] proposed an alternative method to prevent particle clumping. In their approach, marker advection velocity is modified by the gradient of a constant base pressure. Although theoretically zero, the SPH discretization of the gradient of a constant pressure field is not zero due to not being 0th-order consistent. The computational overhead imposed by this technique is less than XSPH since all the extra information can be obtained when calculating the right hand sides of Eqs. (4) and (5).

2 Boundary Condition Enforcing (BCE) markers

The state update of any SPH marker relies on the properties of its neighbors and resolves shear as well as normal inter-marker forces. For the SPH markers close to solid surfaces, the SPH summations presented in Eqs. (4), (5) capture the contribution of fluid markers. The contribution of solid objects is calculated via Boundary Condition Enforcing (BCE) markers placed on and close to the solid's surface as shown in Figure 1.

Two approaches were considered herein to implement boundary condition using BCE markers. In the first approach, *Approach 1*, the velocity of a BCE marker is obtained from the rigid body motion of the solid and as such it ensures the no-slip condition on the solid surface. Including BCE markers in the SPH summation equations, i.e. Eqs. (4) and (5), results in fluid-solid interaction forces that are added to both fluid and solid markers. The pressure of each BCE marker is obtained through a projection from the fluid domain [4],

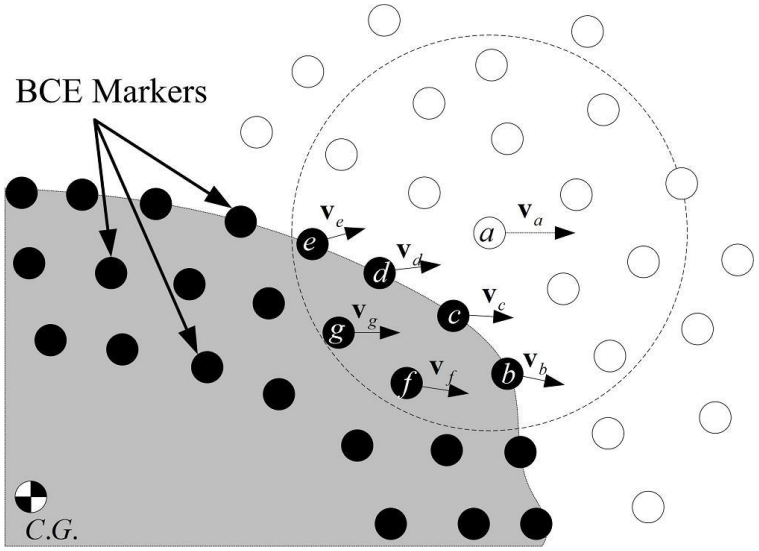

Figure 1: BCE and fluid markers, key for the coupling between fluid and solid, are represented by black and white circles, respectively. A section of the rigid body is shown herein as the gray area. The BCE markers positioned in the interior of the body (markers g and f in the figure) are placed at a depth less than or equal to the size of the compact support associated with the kernel function W.

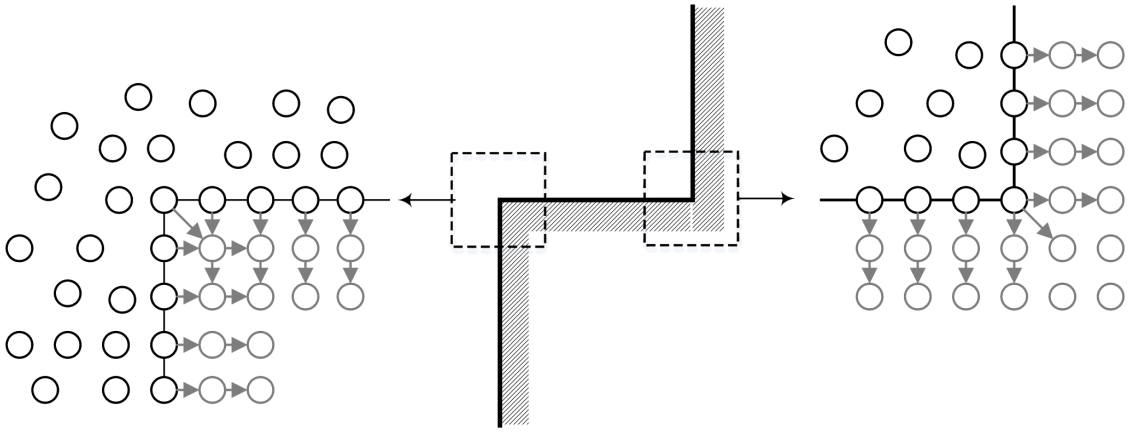

Figure 2: Calculating the wall markers pressure as suggested in [4]. The pressure of a markers located on the wall is calculated similar to the fluid markers and then projected to the interior wall markers. For an external corners, a wall marker may be influenced from several surfaces; therefore, the final pressure is an average of partial contributions.

see Figure 2. For arbitrary geometries, the pressure of each BCE marker is replaced by the pressure of the closest fluid marker.

Once the fluid-solid interaction between individual markers, i.e., the right hand side of Eqs. (4) and (5), is accounted for, the total rigid body force and torque due to the

interaction with the fluid can be obtained by respectively summing the individual forces and their induced torques over the entire rigid body. They are then added to the other forces, including external and contact forces.

In the second approach considered herein [1], *Approach 2*, the velocity of a BCE marker, $\mathbf{v}_a$, is calculated according to

$$\mathbf{v}_a = 2\mathbf{v}_a^p - \tilde{\mathbf{v}}_a, \tag{9}$$

where a denotes a BCE marker, $\mathbf{v}_a^p$ is the prescribed wall velocity, and $\tilde{\mathbf{v}}_a$ is an extrapolation of the smoothed velocity field of the fluid phase to the BCE markers,

$$\tilde{\mathbf{v}}_a = \frac{\sum\limits_{b\in\mathbb{F}} \mathbf{v}_b W_{ab}}{\sum\limits_{b\in\mathbb{F}} W_{ab}}. \tag{10}$$

In Eq. (10), $\mathbb{F}$ denotes the set of fluid markers overlapping the location of marker a.

The pressure of a BCE marker draws on a force balance at the wall interface, which is calculated as

$$p_a = \frac{\sum\limits_{b\in\mathbb{F}} p_b W_{ab} + (\mathbf{g} - \mathbf{a}_a) \cdot \sum\limits_{b\in\mathbb{F}} \rho_b \mathbf{r}_{ab} W_{ab}}{\sum\limits_{b\in\mathbb{F}} W_{ab}}, \tag{11}$$

where $\mathbf{g}$ and $\mathbf{a}_w$ are the gravity and wall accelerations. Although it might not be as accurate as the method proposed in [8], the generalized BCE method [1] given by Eqs. (9) and (11) can be easily applied to arbitrary geometries.

3 Numerical simulations

Two case studies were conducted herein to compare the two approaches. The first study aims at demonstrating the no-slip condition in both approaches used to enforce a wall boundary condition. The second case demonstrate how well the two approaches enforce the non-penetration condition.

3.1 Transient Poiseuille flow

The exact solution for transient Poiseuille flow is provided in [8]. The numerical results of this simulation obtained using *Approach 1* and *Approach 2* are provided along with the exact solution in Figure 3. Except the BCE implementation methodology, all of the simulation parameters were the same in both simulations: the simulation setup consists of a 3D channel with dimensions $(l_x, l_y, l_z) = (1, 0.2, 1)$ mm and confining walls in the z direction. Periodic boundary conditions were considered in the x and y directions to generate a 2D flow in the $x - z$ plane. The flow is driven by a volumetric acceleration, $\mathbf{f} = 0.1$ m/s^2 $\hat{\mathbf{i}}$. The results

show that both approaches are capable of producing correct velocity profiles by imposing a reasonable no-slip condition at the wall. It is worth mentioning that $t \to \infty$, i.e the time for the final curve, is just a simulation time that is large enough to produce a fully developed velocity profile. As it was shown in [10], numerical errors, caused by an improper use of particle initial spacing to resolution length ratio, can blunt the velocity profile after a long simulation time. This problem, however, can be alleviated by reducing the inter-particle spacing.

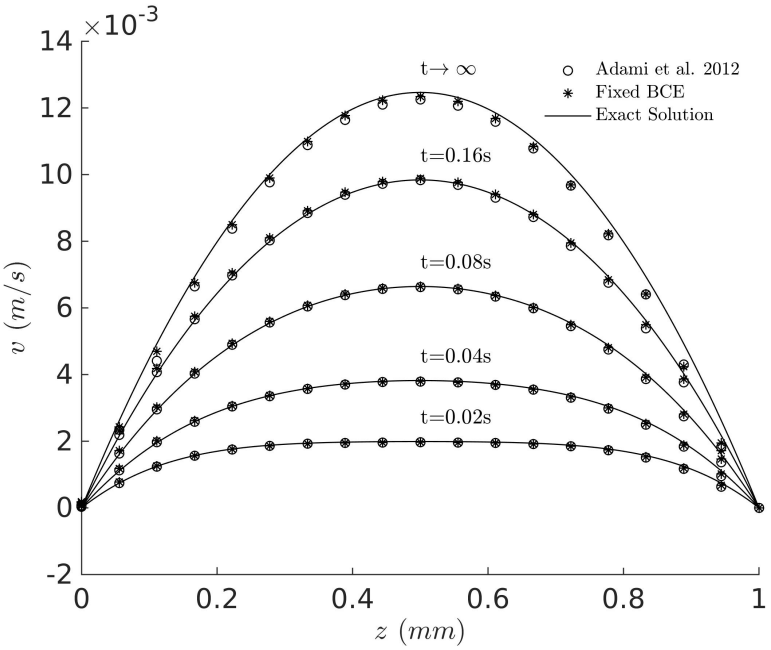

Figure 3: Transient Poiseuille flow solution obtained from *Approach 1* (∗), *Approach 2* (o), and exact solution (solid line). No-slip condition is satisfied by both simulation approaches.

3.2 Fluid under gravity

In the second test, we measure the efficiency of the fixed BCE markers in preventing the marker boundary-penetration under gravity. For such situations, i.e. those under gravity or other strong external forces, it is suggested to use a molecular dynamics like force, such as van der Waals, between fluid and boundary markers [6].

The problem of boundary penetration can appear at the later stages of the simulation as the fluid velocity changes from still. To be able to see this problem at earlier stages of the simulation, a column of water was created in a bucket, see Figure 4. The fluid was given a certain velocity downward, in the direction of the gravity. This setup mimics a column of fluid dropped from a certain height – a scenario encountered in many practical applications – including dam break. Two tests were performed herein: in the first test, *test 1*, a fixed BCE scheme without any artificial force was used; alternatively, *Approach 2* was leveraged in the

second test, *test 2*. As shown in Figure 4a, the fixed BCE approach used in *test 1* cannot sufficiently block the particles penetration. This problem, however, can be well resolved using *Approach 2*, as it modifies the boundary pressure based on a local force balance, see Figure 4b.

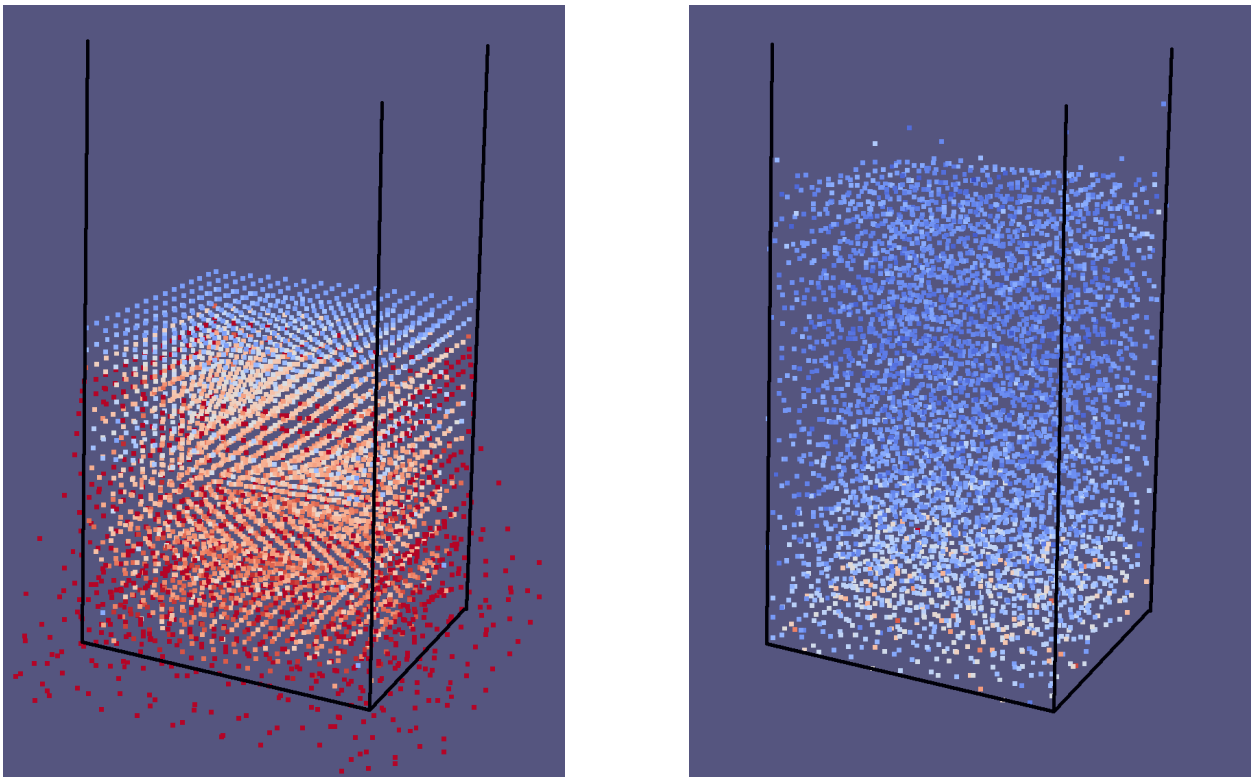

(a) (b)

Figure 4: Test of boundary condition for no-penetration under gravity. While all simulation parameters were maintained similar, two different BCE approaches were used: (a) *Approach 1* (fixed BCE approach); (b) *Approach 2* [1]. The colors represent the markers pressure, with red and blue being the maximum and minimum pressures, respectively. The result show a clear advantage when *Approach 2* is leveraged.

4 Conclusion

We compared two different approaches to impose a solid boundary condition. Both approaches rely on a boundary discretization using BCE markers. In the first approach, the velocity of a BCE marker is obtained from the kinematics of the boundary at the location of the marker. This implies that the BCE marker is fixed to the boundary. The pressure of a BCE marker is obtained by replicating the local fluid pressure in the boundary normal direction. In the second approach, BCE velocities are re-defined at each time step such that

the local solid velocity is reproduced when combining the BCE and fluid contributions at the BCE location. complemented by fluid contribution, they can re-produce the local solid velocity. Therein, the boundary pressure is obtained from a force balance at the interface.

Through the simulation of a transient Poiseuille flow, we showed that both approaches are capable of maintaining the no-slip condition at the boundary. However, the second approach is advantageous in maintaining the non-penetration condition. To demonstrate this, we set up a simulation containing a gravitational field, and showed that non-penetration condition is violated in the fixed BCE approach (*Approach 1*) unless an artificial force is considered at the interface. On the contrary, the second approach (*Approach 2*) successfully impose the non-penetration condition without any artificial treatment.

Acknowledgement

The authors would like to thank Milad Rakhsha for his comments on a draft of this manuscript.

References

[1] S Adami, XY Hu, and NA Adams. A generalized wall boundary condition for smoothed particle hydrodynamics. *Journal of Computational Physics*, 231(21):7057–7075, 2012.

[2] GK Batchelor. *An introduction to fluid mechanics*. Cambridge University Press, 1974.

[3] Robert H Cole. Underwater explosions. *Physics Today*, 1(6):35–35, 2009.

[4] E.S. Lee, C. Moulinec, R. Xu, D. Violeau, D. Laurence, and P. Stansby. Comparisons of weakly compressible and truly incompressible algorithms for the SPH mesh free particle method. *Journal of Computational Physics*, 227(18):8417–8436, 2008.

[5] J. J. Monaghan. On the problem of penetration in particle methods. *Journal of Computational Physics*, 82(1):1–15, 1989.

[6] J. J. Monaghan. Smoothed Particle Hydrodynamics. *Reports on Progress in Physics*, 68(1):1703–1759, 2005.

[7] Joseph J Monaghan and John C Lattanzio. A refined particle method for astrophysical problems. *Astronomy and astrophysics*, 149:135–143, 1985.

[8] J P Morris, P J Fox, and Y Zhu. Modeling low Reynolds number incompressible flows using SPH. *Journal of Computational Physics*, 136(1):214–226, 1997.

[9] A Pazouki and D Negrut. A numerical study of the effect of particle properties on the radial distribution of suspensions in pipe flow. *Computers & Fluids*, 108:1 – 12, 2015.

[10] Baofang Song, Arman Pazouki, and Thorsten Pöschel. Instability of SPH applied to poiseuille flow. *under preparation*, 2015.